

Accepted Manuscript

Nucleation and self-assembly dynamics of hierarchical $\text{YAIO}_3:\text{Ce}^{3+}$ architectures: Nano probe for in vitro dermatoglyphics and anti-mimetic applications

G.P. Darshan, H.B. Premkumar, H. Nagabhushana, S.C. Sharma, B. Umesh, R.B. Basavaraj



PII: S0928-4931(18)32102-7
DOI: <https://doi.org/10.1016/j.msec.2019.01.060>
Reference: MSC 9318
To appear in: *Materials Science & Engineering C*
Received date: 19 July 2018
Revised date: 13 January 2019
Accepted date: 14 January 2019

Please cite this article as: G.P. Darshan, H.B. Premkumar, H. Nagabhushana, S.C. Sharma, B. Umesh, R.B. Basavaraj, Nucleation and self-assembly dynamics of hierarchical $\text{YAIO}_3:\text{Ce}^{3+}$ architectures: Nano probe for in vitro dermatoglyphics and anti-mimetic applications. *Msc* (2018), <https://doi.org/10.1016/j.msec.2019.01.060>

This is a PDF file of an unedited manuscript that has been accepted for publication. As a service to our customers we are providing this early version of the manuscript. The manuscript will undergo copyediting, typesetting, and review of the resulting proof before it is published in its final form. Please note that during the production process errors may be discovered which could affect the content, and all legal disclaimers that apply to the journal pertain.

Nucleation and Self-Assembly Dynamics of Hierarchical $\text{YAlO}_3:\text{Ce}^{3+}$ Architectures: Nano Probe for *in vitro* Dermatoglyphics and Anti-Mimetic Applications

G.P. Darshan^{1,2}, H.B. Premkumar^{3,*}, H. Nagabhushana^{4,*}, S.C. Sharma⁵, B. Umesh⁶,
R.B. Basavaraj⁴

¹Department of Physics, Acharya Institute of Graduate Studies, Bangalore 560 107, India

²Research and Development Centre, Bharathiar University, Coimbatore 641 046, India

³Department of Physics, Ramaiah University of applied Sciences, Bangalore 560 054, India

⁴Prof. C.N.R. Rao Centre for Advanced Materials, Tumakuru University,
Tumakuru-572103, India

⁵Director - National Assessment and Accreditation Council, work carried out as Honorary
Professor, Jain University, Jakkasandra Post, Kanakapura Taluk, Ramanagara Dist,
Bangalore 562112, India

⁶Department of Science and humanities, PVP polytechnic, Bangalore 560 056

Abstract

Highly efficient blue emitting $\text{YAlO}_3:\text{Ce}^{3+}$ (1-11 mol %) nanopowders have been fabricated via bio-surfactant Epigallocatechin Gallate assisted ultrasound irradiated sonochemical route. The nucleation and self-assembly dynamics of solids in solutions influences many straightforward normal processes, hence it plays a vital role in materials engineering applications. Nevertheless, the comprehensive nucleation and self-assembly mechanisms of hierarchical architectures still poorly acknowledged. In the present work, we have been exploring the nucleation and stepwise self-assembly dynamics of the $\text{YAlO}_3:\text{Ce}^{3+}$ (5 mol %) nanopowders into hierarchical architectures. We found that under ultrasound irradiation, nucleation in the solution forms via multi step process and self-assembly was stimulated by intermolecular forces between the nanopowders and external forces. The optimized $\text{YAlO}_3:\text{Ce}^{3+}$ (5 mol %) nanopowders used as a luminescent labeling agent for visualization latent fingerprints on various porous and non-porous surfaces under ultraviolet 254 nm light. The obtained results exhibit well defined ridge details with high sensitivity, selectivity and low background hindrance which showed greater advantages as compared to the conventional powders. Extensive fingerprint details, namely the number and distribution of sweat pores in a ridge were clearly revealed. Further, demonstrated the viability of high-performance security labels using optimized sample for practical anti-mimetic applications. The present work, enabling understanding of ultrasound assisted nucleation and self-assembly of nanopowders which impart dermatoglyphics and anti-mimetic applications.

Keywords: Nanopowder; Photoluminescence; Dermatoglyphics; Sweat pores; Anti-mimetic; Hierarchical Architectures.

*Corresponding Authors: Dr. H.B. Premkumar (Email: premhb@gmail.com; Tel: +91-9880433880); Prof. H. Nagabhushana (E-mail: bhushanvlc@gmail.com; Tel: +91-9663177440).

1. Introduction

From past decades, a single step origin of nascent phase (i.e., nucleus) from solution was effectively explained by the classical theory of nucleation (CTN) [1-5]. However, the CTN fails to describe more-complex systems, namely the crystallization rate of Lysozyme and ice [6, 7]. In order to overcome from these inconsistencies, many non-classical theories were presented. One such theory follows multi-step process by forms solute-rich and solute-poor phases undergone by decomposition of precursor solutions. This results in formation of nuclei in a solute-rich phase [8-10]. However, hierarchical architectures were organized by the self-assembly phenomena via efficient bottom-up nanofabrication route using intermolecular interactions and external forces [11, 12]. The hierarchical architectures drive unique properties, namely optical, electronic and mechanical properties, which were quite distinct from their bulk counterpart [13, 14]. Hence, the hierarchical architectures offer a wide range of applications, including bio-sensing, photovoltaic, plasmonic, magnetic, catalysis, etc. [15-18]. Limited efforts have been done in order to understand the physical and chemical dynamics involved in self-assembly of hierarchical architectures in the solutions. The classical Derjaguin-Landau-Verwey-Overbeck (DLVO) theory was used to describe the particle-particle or particle-surface interactions [19]. But, it fails to evident the self-assembly phenomena, when particle size approaches to several nano-regime. Hence alternative pathways were necessitating to demonstrate nanoscale nucleation and self-assembly dynamics.

The scientific study and analysis of latent fingerprints (LFPs) was called dermatoglyphics. The dermatoglyphics plays a vital role for identification of individuals in forensic science. Generally, fingerprints (FPs) available in crime spot investigation were categorized into three types, namely patent, latent and plastic [20-22]. During the crime investigation, most available FPs were latent; visualization of such LFPs was leading

challenge for the forensic experts. Many rigorous efforts have been attempted to visualization of LFPs, but still remain some drawbacks, including low sensitivity, selectivity, high hindrance and high toxicity from patterned or dark backgrounds [23]. Normally, the FP development powder was categorized as regular, metallic and luminescent powders based on its composition and properties [24-26]. The regular powders are combined with adhesive polymers and dye materials. Metallic powders are meshed metal particles, such as gold, silver, etc. Although, regular and metallic FP powders were simple and economic, they suffer from various problems [27]. Hence, many luminescent nanopowders (NPs) were employed to overcome from such limitations. For example, Shao and co-workers synthesized $\text{YVO}_4: \text{Bi}^{3+}, \text{Eu}^{3+}$ NPs by micro-emulsion method. The optimized NPs was utilized to visualize LFPs on many surfaces. The obtained results reveal only few type 1 and type 2 details, including the bifurcation, hook, crease, termination and whorl [28]. In addition, Wang et al. reported that the LFPs visualized by silica coated- NaYF_4 up-conversion nanomaterials reveals only arches and termination detail as well as revelation of sweat pores was poorly acknowledged [29].

From past years, mimetic or counterfeiting of currency and documents significantly increasing, which may cause an economic imbalance of the countries [30, 31]. Hence, several countries spend more budget to overcome counterfeiting activities [32]. Therefore, this field creates numerous interest for the researchers to develop anti-mimetic technologies, such as simple markers, security inks, watermarks, holograms and barcodes. Nevertheless, some of the traditional techniques have major drawbacks, namely hazardous to user health and the opaque nature due to utilization of toxic solvents and materials [33]. To overcome such limitations, soluble luminous materials exhibit high efficiency, high contrast, high selectivity and nontoxicity were quite necessary.

Nanomaterials with specific surface functionality are ubiquitous in nature [34, 35]. The term surfactant-decorated nanoparticles, as used in the chemical sciences is typically associated with man-made nanostructures for applications in imaging, drug delivery, composites, catalysis, energy conversion devices, purification systems, and other technologies [36-38]. A surfactant molecule has a hydrophilic (water-loving) head and a long hydrophobic (water-hating or oil-loving) tail, and includes classic alkyl-based surfactants, peptides, lipids, DNA, molecular ligands, bioconjugates, and polymers covalently grafted to or non-covalently assembled on nanomaterial surfaces, thereby changing their properties [39]. The addition of more surfactants creates a smaller efficiency and possibly diminishes recoalescence. In addition, surfactants often lower the interfacial tension between two or more components in a material system, thereby increasing miscibility, colloidal stability, dispersion, and enabling a wider property portfolio of the multicomponent material [40, 41].

In the present work, hierarchical $\text{YAlO}_3:\text{Ce}^{3+}$ (1-11 mol %) architectures were fabricated via ultrasonication route using Epigallocatechin Gallate (EGCG) as a bio-surfactant. The prepared samples were well characterized and further utilized for dermatoglyphics and anti-mimetic applications.

2. Experimental and Characterization

In the present study, analytical grade chemicals were used without any further purification. Yttrium nitrate hexahydrate [$\text{Y}(\text{NO}_3)_3 \cdot 6\text{H}_2\text{O}$ (99.8 %)], Aluminum nitrate nonahydrate [$\text{Al}(\text{NO}_3)_3 \cdot 9\text{H}_2\text{O}$ (99.9 %)], cerium nitrate hexahydrate [$\text{Ce}(\text{NO}_3)_3 \cdot 6\text{H}_2\text{O}$ (99.9 %)] and EGCG ($\text{C}_{22}\text{H}_{18}\text{O}_{11}$) were purchased from the Sigma Aldrich Co. The appropriate amount of yttrium nitrate, aluminum nitrate and cerium nitrate were uniformly mixed in double deionized water (~ 60 ml) using a magnetic stirrer for ~ 30 min. However, a bio-surfactant EGCG (~ 10 g) was thoroughly mixed in ~ 220 ml distilled water under constant stirring. The obtained EGCG solution was added to reaction solution. To regulate the pH value of the reaction

mixture, NaOH solution was mixed into the precursor solution in a drop wise at the rate of 2 ml/min. A titanium probe sonicator (power ~ 300 W) was placed in a reaction beaker by maintained at a temperature of ~ 70 °C. The precipitate obtained at the end of the reaction was filtered, washed with double distilled water, and dried at ~ 80 °C for 3 h in a hot air oven. The homogeneity of the prepared sample was achieved by subsequent calcination at ~ 1000 °C for ~ 3 h under ambient conditions. The experiment was repeated by varying experimental parameters, namely ultrasound irradiation time and concentration of EGCG. Schematic representation of probable crystallization mechanism in the ultrasonication method was shown in Fig.1 (a).

Well calibrated Shimadzu made X ray diffractometer (Shimadzu 7000) with nickel filter and Cu-K α radiation ($\lambda = 0.15406$ nm) was used for phase purity and structural characterization of the prepared samples. The Fourier transformation infrared (FTIR) spectroscopy was carried out by a Perkin Elmer Spectrometer (Spectrum 1000) with KBr pellets to study the positions of the chemical bonding. The surface morphologies of the materials were studied by scanning electron microscope (SEM, Model No. Hitachi- TM 3000) and transmission electron microscope (TEM, Model No. Hitachi H-8100, Kevex sigma TM Quasar, USA). The photoluminescence (PL) data were recorded using Spectrofluorimeter equipped with Fluorolog- 3 (Jobin Yvon), where a Xenon flash lamp was used as an excitation source.

The FP donor hands were thoroughly washed with water. The tip of the fingers was gently rubbed on the forehead and deposited on various forensic related porous and non-porous surfaces with nominal pressure. To visualize such LFPs, the optimized YAlO $_3$:Ce $^{3+}$ (5 mol %) NPs was stained onto the LFPs area with a feather brush. The excess powder was removed from the surface by smooth brushing until clear FPs patterns were obtained. Finally, the developed FPs were *in situ* photographed using 50 mm f/2.8 G, ED lens Nikon

D3100/AF-S digital camera under 254 nm UV light. Fig.1 (b) shows various steps involved in LFPs visualization technique using optimized $\text{YAlO}_3:\text{Ce}^{3+}$ (5 mol %) NPs followed by powder dusting method.

The anti-mimetic labels were prepared by uniformly adding 0.1 g of the optimized sample with 50 ml PVC gold medium using a magnetic stirrer for ~ 1 hr. The choice of PVC gold medium was provided better adhesive nature and it disperses NPs without any agglomeration. The obtained dispersion was printed on porous paper by dip pen mode and dried in vacuum at ~ 28 °C for 8 h. The printed marks were *in situ* photographed using a digital camera under UV light (254 nm).

3. Results and Discussion

PXRD profiles of $\text{YAlO}_3:\text{Ce}^{3+}$ (1-11 mol %) NPs was depicted in Fig.2 (a). Intense and narrow diffraction peaks confirm the formation of single orthorhombic phase and were in good agreement with standard JCPDS No. 70-1677 [42]. No obvious additional impurity peaks were identified, indicating that the dopant Ce^{3+} ions were effectively substituted in YAlO_3 lattice sites. As seen in Fig.2 (a), a slight shift in the diffraction peak (121) towards the lower angle side, which due to ionic radii mismatch. As per literature, the acceptable percentage difference (D_r) between host and dopant ions should not be greater than 30 %. In the present work, value of D_r between Y^{3+} and Ce^{3+} ion was estimated by using following relation;

$$D_r = \frac{R_s - R_d}{R_s} \text{-----} (1)$$

where, R_d and R_s ; ionic radii of Ce^{3+} ion (1.283 Å) and Y^{3+} site (1.075 Å), respectively. The value of D_r was estimated and obtained to be ~ 16 %, indicating that the dopant Ce^{3+} ions were effectively substituted to Y^{3+} sites in YAlO_3 host.

The broadening in diffraction peaks was commonly connected with crystallite size or the strains present within the sample or both. Hence, the Scherrer's relation was utilized to determine average crystallite size (D) of the prepared NPs, as given below [43];

$$D = \frac{0.9\lambda}{\beta \cos \theta} \text{-----} (2)$$

where β ; full width at half maxima (FWHM), λ ; X-ray wavelength (1.542 Å), θ ; the Bragg's angle. The 'D' values of the prepared NPs were estimated and given in Table 1. Further, the 'D' values and micro strain present in NPs were calculated by utilizing Williamsons - Hall (W-H) equation [44];

$$\frac{\beta \cos \theta}{\lambda} = \frac{1}{D} + \frac{\varepsilon \sin \theta}{\lambda} \text{-----} (3)$$

where ε ; strain associated with NPs. The Eq.3 represents a straight line between $4\sin\theta$ (X-axis) and $\beta\cos\theta$ (Y-axis). The slope and intercept of the line give strain (ε) and 'D' values (Fig. 2 (b)). The average crystallite size of the samples was estimated and listed in Table 1. The variation in 'D' values with different Ce^{3+} ion concentration was shown in Fig.2 (c).

FTIR spectra of $\text{YAlO}_3:\text{Ce}^{3+}$ (1–11 mol %) NPs in the range 500–4000 cm^{-1} was depicted in Fig.2 (d). A peak observed at $\sim 3440 \text{ cm}^{-1}$, ascribed to vibration mode of chemically bonded hydroxyl groups. The slight variation in the intensity of this peak was due to an appreciable reduction in $-\text{OH}$ and $-\text{NH}$ groups in the YAlO_3 . A vibration peak at $\sim 1470 \text{ cm}^{-1}$ was attributed to the bending mode of H–O–H vibrations. The intense peak observed at $\sim 708 \text{ cm}^{-1}$ was due to Al–O stretching of AlO_6 group [45].

The use of ultrasound to initiate chemical reactions in the solution considerably increased due to improved crystallization rate and reduced by-products. The effect of ultrasound arises from formation, growth and impulsive collapse of cavities (i.e., acoustic

cavitation) [46]. When the reaction solution was treated with ultrasound, alternating expansive and compressive acoustic waveforms make cavities to oscillate. The developed cavities will start growing by effective consumption of ultrasonic energy. Under certain conditions, the cavities undergo overgrow and collapse by releasing all stored energy in a short period. This cavity impulsion was confined with a temperature and pressure of ~ 5000 K and 100 bars, respectively. This helps to viable nanocrystal nucleation in a solution with enhanced crystallization rate [47].

The probable nanocrystal nucleation in the solution under ultrasound can be explained by a multi-step process; spinodal decomposition of the precursor solution forms solute-free and solute-rich aqueous phases, nucleation of amorphous clusters in a solute-rich phase and formation of clusters into the crystalline product. The nucleation of hierarchical $\text{YAlO}_3:\text{Ce}^{3+}$ (5 mol %) architecture was initiated in homogeneous precursor solutions in the presence of ultrasound. These precursors remixes into solute -rich and solute-free aqueous phases. The initial aqueous phase can be separated by the generation of solvated electrons due to interaction of high-energy electrons with aqueous solutions. Then, solute-rich phase condenses into amorphous nanoclusters and exhibit several dynamics, namely diffusion, rotation, coalescence and shrinking and/or growing via Ostwald ripening. Finally, amorphous clusters solidify to form a crystalline product. The plausible scheme for formation of hierarchical architectures via multi-step nucleation process was depicted in Fig.3.

Self-assembly was defined as a spontaneous and reversible organization of molecules or atoms into ordered structures by non-covalent interactions. Generally, chemical reactions proceed towards disorder under thermodynamic parameters; however, precipitation reactions, which drive atoms and molecules to assemble into higher ordered structures, also fall within the category of self-assembly. In self-assembly, the ability to control particle size and shape, size distribution, composition and agglomeration essentially requires considerable

understanding of the energetics by which molecules interact and the careful control of the conditions during assembly [48]. This includes understanding molecular affinity and bio-recognition mechanisms, which depends on hydrogen bonding, steric repulsion and geometry, π - π interactions, van der Waals and electrostatic forces. In some cases, self-assembly can be aided with external fields or templates and seeds that enhance the thermodynamic forces driving self-assembly, these are known as directed or guided self-assembly [49]. Bio-surfactant EGCG assisted self-assembly phenomena in the precursor solution was initiated by intermolecular forces between precursors and external forces (i.e., hydrophobic, van der Waals and electrostatic interactions between NPs). The phytochemical EGCG was known to act as both a reducing agent and stabilizer to form crystalline products. The polyphenolic structure of EGCG also contributes a great deal to hydrogen bonding. The formation of large hydration shells occurs via hydrogen bonding with water molecules that result in lower absorption of EGCG [50]. This hydrogen bonding also enables the capacity to bind strongly to proteins and nucleic acids – binding to signaling molecules and receptors, and thus inhibiting the functions of key receptors, kinases, proteinases and other enzymes in relation to nanoparticles within an appropriate range of concentrations and ratios. Further, it has been known that nanoparticles can increase the bioavailability and reduce toxicity [51]. Fig.4 depicts the probable self-assembly mechanism of hierarchical $\text{YAlO}_3:\text{Ce}^{3+}$ (5 mol %) structures. In the present work, ultrasound irradiation and EGCG can guide self-assembly of hierarchical architectures. At lower EGCG concentrations, interaction of NPs and EGCG form micelle structure to reduce the electrostatic repulsion between NPs. When the concentration of EGCG was increased, hierarchical structures form via successive connection of NPs to binding sites situated along the circumference of the EGCG surfactant, followed by arrangement and orientation of the NPs. Probable growth mechanism of $\text{YAlO}_3:\text{Ce}^{3+}$ (5 mol %) hierarchical architectures in the presence of EGCG were shown in Fig.5.

SEM micrographs of Ce^{3+} doped YAlO_3 hierarchical structures prepared by the varying ultrasound irradiation time (1-6 h) was shown in Fig.6 (a-f). It was evident from the figure that, some irregular aggregates act as a building block to form architectures were observed at 1 h ultrasound irradiation time (Fig.6 (a)). When the ultrasound irradiation time increased to 2 h, irregular aggregates fragmented and ordered growth. Further, samples fabricated at prolonged ultrasound irradiation times, i.e., 3 and 4 h, individual fragments will undergo self-assembly to form the bullets like structures (Fig. 6 (c & d)). In addition, when ultrasound irradiation time was increased to 5 and 6 h, bullets like structures will undergo self- assembly in an oriented direction to form hierarchical flower-like architecture (Fig. 6 (e & f)).

However, bio-surfactant EGCG concentration plays a vital role in the formation of flower-like $\text{YAlO}_3:\text{Ce}^{3+}$ (5 mol %) structures. SEM micrographs of the optimized sample fabricated by varying bio-surfactant EGCG concentration was shown in Fig.7 (a-f). When the EGCG concentration was increased to 5 %W/V, irregular shaped flakes like structures were formed (Fig. 7 (a)). As the concentration of EGCG continues to increase to 10 and 15 %W/V, the irregular shaped particles undergo further growth to form hexagonal shaped structures. Further, samples fabricated with 20 – 30 %W/V of EGCG concentration, hexagonal like structures will undergo self- assembly in an oriented direction results hierarchical flower-like architecture (Fig. 7 (d-f)).

TEM image of the optimized $\text{YAlO}_3:\text{Ce}^{3+}$ (5 mol %) NPs was shown Fig. 8 (a). Individual fragments of flower-like architectures were observed. From HRTEM image, interplanar spacing (d) between lattice planes were measured and found to be ~ 0.36 nm for (121) plane (Fig.8 (b & d)). The SAED pattern shows that prepared samples were well-crystallized and consistent with the PXRD analysis. Further, discontinuous ring patterns along with sharp spots indicating the presence of nano - sized particles (Fig.8 (c)).

Fig.9 (a) shows the PL excitation spectrum of $\text{YAlO}_3:\text{Ce}^{3+}$ (5 mol %) NPs by monitoring emission wavelength at ~ 460 nm. A broad spectrum centered at ~ 300 nm, which ascribed to $4f^7 \rightarrow 4f^6 5d^1$ transition of Ce^{3+} ions was observed. The PL emission spectra of $\text{YAlO}_3:\text{Ce}^{3+}$ (1–11 mol %) NPs excited at ~ 300 nm at room temperature was shown in Fig. 9 (b). The emission spectra exhibit intensive, broad peak centered at ~ 460 nm (cyan color), which may due to $^5\text{D}_{3/2} \rightarrow ^7\text{F}_{7/2}$ transitions of Ce^{3+} ions. Normally, luminescent property of the NPs was mainly reliant on the dopant concentration. Variation of PL intensity with dopant Ce^{3+} ion concentration was depicted in Fig. 9 (c). It was evident that from the figure that, no obvious change in the emission profiles, except the emission intensity. The PL emission intensity enhances with an increase of Ce^{3+} ion concentration up to 3 mol % and later diminishes. This diminished PL intensity was mainly attributed to concentration quenching. Generally, the concentration quenching phenomena may be caused due to defect to dopant Ce^{3+} energy transfer, phonon assisted energy transfer by electron – phonon coupling and Ce^{3+} - Ce^{3+} transfer [52]. In our work, absence of defect to Ce^{3+} energy transfer transition and phonon assisted transition, suggesting that these kind of energy transfer was not responsible for the concentration quenching phenomena. Hence, determination of non-radiative energy transfers among dopant Ce^{3+} ions was mainly liable for concentration quenching was necessary, which commonly happens as a consequence of an exchange interaction, radiation absorption, or a multipole–multipole (m-m) interaction. According to Blasse, type of interaction can be predicted by estimating the critical distance (R_c) among Ce^{3+} ions by using the following equation;

$$R_c = 2 \left[\frac{3V}{4\pi XN} \right]^{1/3} \text{-----(4)}$$

where V; unit cell volume, X; optimized Ce^{3+} ion concentration and N; number of ions per unit cell. In our work, value of R_c was estimated and found to be ~ 12.26 Å. The obtained

value of the R_c greater than 5 \AA , results that the m–m interaction was prominent. The obtained result indicating that the m-m interaction is the main reason for concentration quenching. To reveal the type of m-m interaction mechanism intricate in the energy transfer among dopant Ce^{3+} ions was estimated by Dexter and Schulman relation;

$$\frac{I}{X} = \frac{k}{\beta X^{s/3}} \text{-----(5)}$$

where X ; activator concentration, k and β ; constants for a specific concentration, and s ; values corresponding exchange, dipole–dipole, dipole–quadrupole, quadrupole–quadrupole interactions were 6, 8 and 10, respectively. The slope ($s/3$) of linearly fitted plot of $\log(I/x)$ vs $\log(x)$ was found to be -0.6521 (Fig. 9 (d)). The estimated value of Q was obtained to be ~ 6.43 , which was almost equal to the theoretical value of 6 for dipole–dipole interaction. This entails that the dipole–dipole interaction was a main interaction mechanism for concentration quenching.

The photometric properties of $\text{YAlO}_3:\text{Ce}^{3+}$ (1–11 mol %) NPs was estimated by using emission intensity and corresponding wavelengths. It was noticed that the estimated International Commission on Illumination (CIE) coordinate values were situated in the blue region of the chromaticity diagram. Further, correlated color temperature (CCT) values were also estimated using the standard relation described elsewhere [53, 54]. The CIE, CCT diagrams and their corresponding coordinates were given in (Fig. 9 (e & f)).

Fig.10 depicts the visualized LFPs on various backgrounds coloured porous surfaces by staining the optimized $\text{YAlO}_3:\text{Ce}^{3+}$ (5 mol %) NPs excited at 254 nm UV light. Well defined and bright ridge characteristics were clearly revealed without any color disruption after UV 254 nm light irradiation, exhibit outstanding contrast for LFPs visualization due to its nano-regime. In order to determine the superiority of the optimized sample to visualize LFPs, conventional FPs powders, namely magnetic iron oxide and TiO_2 powders were used as a control (Fig.11 (a-c)). The obtained results evident that the conventional powders could

not reveal many details. Table.2 depicts the several hosts have been used to visualize LFPs on different surfaces. However, FPs stained by the optimized NPs were clearly revealed various ridge details with sharp edges, showing that prepared $\text{YAlO}_3:\text{Ce}^{3+}$ (5 mol %) NPs could be used as an effective powder for the visualization of latent fingerprints due to their enhanced strong blue luminescence.

Furthermore, in order to demonstrate the stability of the $\text{YAlO}_3:\text{Ce}^{3+}$ (5 mol %) NPs based LFPs visualization method in forensic sciences, we conducted the LFPs visualization experiments after the FPs had been aged for different periods of time. As shown in Fig.11 (d-g), the detection sensitivity decreased gradually with prolonged aging of the FPs, due to the gradual evaporation of the constituents present in the FPs. However, LFPs aged for up to 30 days could still be developed with clear ridges, indicating that the stability of the $\text{YAlO}_3:\text{Ce}^{3+}$ (5 mol %) NPs was high enough for aged FPs development. Hence, optimized sample was considered to be an exceptionally likely replacement for traditional FP powders.

Subsequent trials were performed to determine the practicability of the prepared NPs. Visualized FPs images by optimized $\text{YAlO}_3:\text{Ce}^{3+}$ (5 mol %) NPs on many surfaces, namely glass, pattern plastic sheet, marble, mica sheet, stainless steel and computer mouse under UV 254 nm light was shown in Fig.12. Detailed ridge characteristics of the FPs, including whorl, bi-furcation, bridge, dot, hook, island, trifurcation, and ridge end can be clearly revealed (Fig.12). Generally, level III details such as sweat pores constitute with known chemical compositions offered a unique information which leads to precise and strong evidence in crime investigation. Hence, analysis of sweat pores in FPs becomes more significant. Regrettably, sweat pores were most neglected part owing to the fact that quick, consistent and inexpensive visualization powder have not been developed. Comparison of FP results reported in the previous works with present study was given in Table.3. As evident from the table that, the optimized $\text{YAlO}_3:\text{Ce}^{3+}$ (5 mol %) NPs quite useful for revelation of sweat

pores present in FPs. Close assessment of visualized FPs contains permanent, immutable and unique sweat pores that were presented on the ridges. Visualized pores were nearly rounds with different sizes and are located at the edge of ridges. The obtained results clearly demonstrating that the number and distribution of a pore were unique in a ridge. Hence, the followed protocol not only provides level I-II details of FPs but also enabled the sweat pores to establish the individuality of FPs (Fig.13).

In addition, anti-mimetic application of optimized $\text{YAlO}_3:\text{Ce}^{3+}$ (5 mol %) NPs based ink followed by simple dip pen writing mode under normal and 254 nm UV light illumination was shown in Fig.14. The obtained images were indistinct in a normal light while corresponding images under UV 254 nm light illumination were clear and intense. The obtained results endorse the anti-mimetic applications of the optimized product.

4. Conclusions

Highly luminescent $\text{YAlO}_3:\text{Ce}^{3+}$ (1-11 mol %) NPs were successfully synthesized via ultrasound assisted sonochemical route using EGCG as a bio-surfactant. Intense and narrow diffraction peaks in the PXRD profile confirms the formation of single orthorhombic phase. The nucleation, growth and self-assembly of particles were studied thoroughly by witnessing the morphological variations in various experimental conditions. The rapid nucleation and morphological progression of hierarchical $\text{YAlO}_3:\text{Ce}^{3+}$ (1-11 mol %) architectures were due to production of extraordinary pressure and temperature at the boundary between a collapsing bubble and the bulk solution induced by ultrasound. Plausible formation mechanism of hierarchical structures was proposed based on nucleation, growth, self-assembly and Ostwald ripening process. The PL emission spectra exhibit intensive, broad peak centered at ~ 460 nm (cyan color), which may due to $^5\text{D}_{3/2} \rightarrow ^7\text{F}_{7/2}$ transitions of Ce^{3+} ions. The PL emission intensity enhances with an increase of Ce^{3+} ion concentration up to 3 mol % and later diminishes, which attributed to concentration quenching phenomena. The detailed FPs features such as a whorl, eye, bi-furcation, dot, island, ridge ending and bridge can be clearly revealed. In addition, most neglected sweat pores and their numbers and distribution of a pore could thus be clearly revealed. A few such level 3 details offered an exceptional evidence, which was enough to find a human individuality in a crime scene investigation. Hence, the optimized NPs can be regarded as a promising cyan blue phosphor material, which endorse applications in advanced forensic and anti-mimetic fields.

References

1. N. Duane Loh, Soumyo Sen, Michel Bosman, Shu Fen Tan, Jun Zhong, Christian A. Nijhuis, Petr Král, Paul Matsudaira, Utkur Mirsaidov, Multistep nucleation of nanocrystals in aqueous solution, *Nature Chem.*, DOI: 261810.1038/NCHEM.2618.
2. R.P. Sear, The non-classical nucleation of crystals: microscopic mechanisms and applications to molecular crystals, ice and calcium carbonate. *Int. Mater. Rev.*, 57 (2012) 328-356.
3. J. J. De Yoreo, P. G. Vekilov, *Biomineralization* (eds Dove, P., De Yoreo, J. & Weiner, S.) 57–93 (Mineralogical Society of America, 2003).
4. P. G. Vekilov, Dense liquid precursor for the nucleation of ordered solid phases from solution. *Cryst. Growth Des.*, 4 (2004) 671-685.
5. J. J. De Yoreo, James J. De Yoreo, Pupa U. P. A. Gilbert, Nico A. J. M. Sommerdijk, R. Lee Penn, Stephen Whitelam, Derk Joester, Hengzhong Zhang, Jeffrey D. Rimer, Alexandra Navrotsky, Jillian F. Banfield, Adam F. Wallace, F. Marc Michel, Fiona C. Meldrum, Helmut Cölfen, Patricia M. Dove, Crystallization by particle attachment in synthetic, biogenic, and geologic environments, *Science*, 349 (2015) 6760.
6. P. G. Vekilov, The two-step mechanism of nucleation of crystals in solution. *Nanoscale*, 2 (2010) 2346-2357.
7. E. Sanz, Homogeneous ice nucleation at moderate supercooling from molecular simulation, *J. Am. Chem. Soc.*, 135 (2013) 15008-15017.
8. J. De Yoreo, Crystal nucleation: more than one pathway, *Nat. Mater.*, 12 (2013) 284-285.
9. D. Erdemir, A.Y. Lee, A.S. Myerson, Nucleation of crystals from solution: classical and two-step models, *Acc. Chem. Res.*, 42 (2009) 621-629.
10. J.W. Cahn, J. E. Hilliard, Free energy of a non-uniform system: Nucleation in a two-component incompressible fluid, *J. Chem. Phys.*, 31 (1959) 688-699.
11. Y. Min, M. Akbulut, K. Kristiansen, Y. Golan, J. Israelachvili, The role of interparticle and external forces in nanoparticle assembly, *Nat. Mater.*, 7 (2008) 527-538.
12. C. A. S. Batista, R. G. Larson, N. A. Kotov, Non additivity of nanoparticle interactions, *Science*, 350 (2015) 1242477.
13. L. Wang, L. Xu, H. Kuang, C. Xu, N. A. Kotov, Dynamic nanoparticle assemblies, *Acc. Chem. Res.*, 45 (2012) 1916-1926.
14. Z. Nie, A. Petukhova, E. Kumacheva, Properties and emerging applications of self-assembled structures made from inorganic nanoparticles, *Nat. Nanotechnol.*, 5 (2010) 15-25.
15. S.F. Tan, L. Wu, J.K.W. Yang, P. Bai, M. Bosman, C.A. Nijhuis, Quantum plasmon resonances controlled by molecular tunnel junctions, *Science*, 343 (2014) 1496-1499.
16. Z. Nie, A. Petukhova, E. Kumacheva, Properties and emerging applications of self-assembled structures made from inorganic nanoparticles, *Nat. Nanotechnol.*, 5 (2010) 15-25.

17. G. Singh, H. Chan, A. Baskin, E. Gelman, N. Reppin, P. Král, R. Klajn, Self-assembly of magnetite nanocubes into helical superstructures, *Science*, 345 (2014) 1149-1153.
18. M.A. Boles, M. Engel, D.V. Talapin, Self-assembly of colloidal nanocrystals: From intricate structures to functional materials, *Chem. Rev.*, 116 (2016) 11220-11289.
19. J.N. Israelachvili, Thermodynamic and statistical aspects of intermolecular forces in intermolecular and surface forces, Third ed.; Academic Press: San Diego, (2011) 23-51.
20. M. Wang, M. Li, M. Yang, X. Zhang, A. Yu, Y. Zhu, P. Qiu, C. Mao, NIR-induced highly sensitive detection of latent fingerprints by NaYF₄: Yb, Er up-conversion nanoparticles in a dry powder state, *Nano Res.*, 8 (2015) 1800-1810.
21. G.S. Sodhi, J. Kaur, Powder method for detecting LFPs: A review, *Forensic Sci. Int.*, 120 (2001) 172-176.
22. G.P. Darshan, H.B. Premkumar, H. Nagabhushana, S.C. Sharma, B. Daruka Prasad, S.C. Prashantha, R.B. Basavaraj, Superstructures of doped yttrium aluminates for luminescent and advanced forensic investigations, *J. Alloys Compd.*, 686 (2016) 577-587.
23. S.J. Park, J.Y. Kim, J.H. Yim, N.Y. Kim, C.H. Lee, S.J. Yang, H.K. Yang, The effective fingerprint detection application using Gd₂Ti₂O₇:Eu³⁺ nanophosphors, *J. Alloys Compd.*, <https://doi.org/10.1016/j.jallcom.2018.01.116>.
24. R.B. Basavaraj, H. Nagabhushana, G.P. Darshan, B. Daruka Prasad, M. Rahul, S.C. Sharma, R. Sudaramani, K.V. Archana, Red and green emitting CTAB assisted CdSiO₃:Tb³⁺/Eu³⁺ nanopowders as fluorescent labeling agents used in forensic and display applications, *Dyes Pigm.*, 147 (2017) 364-377.
25. K.N. Venkatachalaiah, H. Nagabhushana, G.P. Darshan, R.B. Basavaraj, B. Daruka Prasad, Novel and highly efficient red luminescent sensor based SiO₂@Y₂O₃:Eu³⁺, M⁺ (M⁺ = Li, Na, K) composite core-shell fluorescent markers for latent fingerprint recognition, security ink and solid state lightning applications, *Sens. Actuators, B*, 251 (2017) 310-325.
26. M. Wang, M. Li, A. Yu, J. Wu, C. Mao, Rare earth fluorescent nanomaterials for enhanced development of LFPs, *ACS Appl. Mater. Interfaces*, 7 (2015) 28110-28115.
27. R.B. Basavaraj, H. Nagabhushana, G.P. Darshan, B. Daruka Prasad, M. Rahul, S.C. Sharma, R. Sudaramani, K.V. Archana, Red and green emitting CTAB assisted CdSiO₃: Tb³⁺/Eu³⁺ nanopowders as fluorescent labeling agents used in forensic and display applications, *Dyes Pigm.*, 147 (2017) 364-377.
28. Jingyu Shao, Jinghui Yan, Xiaoguang Li, Shuang Li, Tao Hu, Novel fluorescent label based on YVO₄: Bi³⁺, Eu³⁺ for latent fingerprint detection, *Dyes Pig.*, 160 (2019) 555-562.
29. Lijia Wang, Wenhong Gu, Zhengbin An, Qingyun Cai, Shape-controllable synthesis of silica coated core/shell upconversion nanomaterials and rapid imaging of latent fingerprints, *Sens. Actuators, B*, 266 (2018) 19-25.
30. Wu, Y. Zhong, B. Chu, B. Sun, B. Song, S. Wu, Y. Su, Y. He, Plant-derived fluorescent silicon nanoparticles featuring excitation wavelength-dependent fluorescence spectra for anti-counterfeiting applications, *Chem. Comm.*, 52 (2016) 7047-7050.
31. Zhenyu Sun, Jiakuan Yang, Linwei Huai, Wenxiang Wang, Zhidong Ma, Jika Sang, Jiachi Zhang, Huihui Li, Zhipeng Ci, Yuhua Wang, A spy must be spotted: a multi-stimuli-responsive luminescent material for dynamic multimodal anticounterfeiting and encryption, *ACS Appl. Mater. Interfaces*, (2018) DOI: 10.1021/acsami.8b08977.

32. W. Tian, J. Zhang, J. Yu, J. Wu, J. Zhang, J. He, F. Wang, Phototunable full-color emission of cellulose-based dynamic fluorescent materials. *Adv. Funct. Mater.*, 28 (2017) 1703548.
33. G.P. Darshan, H.B. Premkumar, H. Nagabhushana, S.C. Sharma, S.C. Prashantha, H.P. Nagaswarupa, B. Daruka Prasad, Blue light emitting ceramic nano-pigments of Tm^{3+} doped $YAlO_3$: Applications in latent finger print, anti-counterfeiting and porcelain stoneware, *Dyes Pigm.*, 131 (2016) 268-281.
34. P.D. Howes, R. Chandrawati, M.M. Stevens, Colloidal nanoparticles as advanced biological sensors, *Science*, 346 (2014) 1247390.
35. Kevin C.-W. Wu, Yusuke Yamauchi, Controlling physical features of mesoporous silica nanoparticles (MSNs) for emerging applications, *J. Mater. Chem.*, 22 (2012) 1251-1256.
36. Hongjing Wang, Hu Young Jeong, Nobuhisa Fujita, Toen Castle, Osamu Terasaki, Yusuke Yamauchi, Shape- and size-controlled synthesis in hard templates: Sophisticated chemical reduction for mesoporous monocrystalline platinum nanoparticles, *J. Am. Chem. Soc.* 133 (2011) 14526-14529.
37. J. Nicolas, S. Mura, D. Brambilla, N. Mackiewicz, P. Couvreur, Design, functionalization strategies and biomedical applications of targeted biodegradable/biocompatible polymer-based nanocarriers for drug delivery, *Chem. Soc. Rev.*, 42 (2013) 1147-1235.
38. Kevin C.-W. Wu, Xiangfen Jiang, Yusuke Yamauchi, New trend on mesoporous films: precise controls of one-dimensional (1D) mesochannels toward innovative applications, *J. Mater. Chem.* 21 (2011) 8934-8939.
39. P.J.M. Smeets, K.R. Cho, R.G.E. Kempen, N. Sommerdijk, J.J. De Yoreo, Calcium carbonate nucleation driven by ion binding in a biomimetic matrix revealed by in situ electron microscopy, *Nature Mat.*, 14 (2015) 394-399.
40. Haibo Tan, Yunqi Li, Xiangfen Jiang, Jing Tang, Zhongli Wang, Huayu Qian, Peng Mei, Victor Malgras, Yoshio Bando, Yusuke Yamauchi, Perfectly ordered mesoporous iron-nitrogen doped carbon as highly efficient catalyst for oxygen reduction reaction in both alkaline and acidic electrolytes, *Nano Energy*, 36 (2017) 286-294.
41. Yunqi Li, Bishnu Prasad Bastakoti, Masataka Imura, Soo Min Hwang, Ziqi Sun, Jung Ho Kim, Shi Xue Dou, Yusuke Yamauchi, Synthesis of mesoporous TiO_2/SiO_2 hybrid films as an efficient photocatalyst by polymeric micelle assembly, *Chem. Eur. J.* 20 (2014) 6027-6032.
42. H.B. Premkumar, D.V. Sunitha, H. Nagabhushana, S.C. Sharma, B.M. Nagabhushana, C. Shivakumara, J.L. Rao, R.P.S. Chakradhar, Synthesis, characterization, EPR, photo and thermoluminescence properties of $YAlO_3:Ni^{2+}$ nanophosphors, *J. Lumin.*, 135 (2013) 105-112.
43. H.B. Premkumar, B.S. Ravikumar, D.V. Sunitha, H. Nagabhushana, S.C. Sharma, M.B. Savitha, S. Mohandas Bhat, B.M. Nagabhushana, R.P.S. Chakradhar, Investigation of structural and luminescence properties of Ho^{3+} doped $YAlO_3$ nanophosphors synthesized through solution combustion route, *Spectrochim. Acta Part A: Mol. Biomol. Spect.*, 115 (2013) 234-243.
44. M. Venkataravanappa, H. Nagabhushana, G.P. Darshan, B. Daruka Prasad, G.R. Vijayakumar H.B. Premkumar, Udayabhanu, Novel EGCG assisted ultrasound synthesis of self-assembled $Ca_2SiO_4:Eu^{3+}$ hierarchical superstructures: Photometric characteristics and LED applications, *Ultras. Sonochem.*, 33 (2016) 226-239.
45. H.B. Premkumar, D.V. Sunitha, H. Nagabhushana, S.C. Sharma, B.M. Nagabhushana, C. Shivakumara, J.L. Rao, R.P.S. Chakradhar, Thermoluminescence,

- photoluminescence and EPR studies on Mn^{2+} activated yttrium aluminate ($YAlO_3$) perovskite, *J. Lumin.*, 132 (2012) 2409-2415.
46. K. S. Suslick, S. J. Doktycz, in *Advances in Sonochemistry*, Vol. 1 (Ed.:T. J. Mason), JAI Press, New York 1990, pp. 197.
 47. K. S. Suslick, *Sonochemistry, Science*, 247 (1990) 1439-1445.
 48. Linda Sage, *Dissecting the kinetics of self-assembly*, *Anal. Chem.*, 81 (2009) 3-3.
 49. Xiaoyan Zheng, Lizhe Zhu, Xiangze Zeng, Luming Meng, Lu Zhang, Dong Wang, Xuhui Huang, *Kinetics-controlled amphiphile self-assembly processes*, *J. Phys. Chem. Lett.*, 8 (8) (2017) 1798-1803.
 50. S. Valcic, J.A. Burr, B. N. Timmermann, D. C. Liebler, *Antioxidant chemistry of green tea catechins. New oxidation products of (-)-epigallocatechin gallate and (-)-epigallocatechin from their reactions with peroxy radicals*, *Chem. Res. Toxicol.*, 13 (2000) 801-810.
 51. S. A. B. E. Van Acker, L. M. H. Koymans, Aalt Bast, *Molecular pharmacology of vitamin: structural aspects of antioxidant activity*, *Free Rad. Biol. Med.*, 20 (1996) 331-342.
 52. M. Chowdhury and S. K. Sharma, *Spectroscopic behavior of Eu^{3+} in SnO_2 for tunable red emission in solid state lighting devices*, *RSC Adv.*, 5 (2015) 51102-51109.
 53. S. Som, A. K. Kunti, V. Kumar, V. Kumar, S. Dutta, M. Chowdhury, S. K. Sharma, J. J. Terblans, H. C. Swart, *Defect correlated fluorescent quenching and electron phonon coupling in the spectral transition of Eu^{3+} in $CaTiO_3$ for red emission in display application* *J. Appl. Phys.* 115 (2014) 193101-193114.
 54. *Publication CIE no 15.2, Colorimetry, second ed.*, Central Bureau of the Commission Internationale de L'Eclairage, Vienna, Austria, 1986.
 55. Jin Young Park, Sung Jun Park, Minseok Kwak, Hyun Kyoung Yang, *Rapid visualization of latent fingerprints with Eu-doped $La_2Ti_2O_7$* , *J. Lumin.*, 201 (2018) 275-283.
 56. L. Krishna Bharat, Goli Nagaraju, Jae Su Yu, *Hexadentate ligand-assisted wet-chemical approach to rare-earth free self-luminescent cocoon-shaped barium orthovanadate nanoparticles for latent fingerprint visualization*, *Sens. Actuators, B*, 271 (2018) 164-173.
 57. K.R. Venkatesha Babu, C.G. Renuka, R.B. Basavaraj, G.P. Darshan, H. Nagabhushana, *One pot synthesis of $TiO_2:Eu^{3+}$ hierarchical structures as a highly specific luminescent sensing probe for the visualization of latent fingerprints*, *J. Rare Earths*, <https://doi.org/10.1016/j.jre.2018.05.019>.
 58. M. Dhanalakshmi, R.B. Basavaraj, G.P. Darshan, S.C. Sharma, H. Nagabhushana, *Pivotal role of fluxes in $BaTiO_3:Eu^{3+}$ nano probes for visualization of latent fingerprints on multifaceted substrates and anti-counterfeiting applications*, *Microchem. J.* 145 (2019) 226-234.
 59. Sung Jun Park, Jin Young Park, Hyun Kyoung Yang, *Luminescence of a novel cyan emitting $Sr_{10}(PO_4)_6O:Ce^{3+}$ phosphor for visualization of latent fingerprints and anti-counterfeiting applications*, *Sens. Actuators, B*, 262 (2018) 542-554.
 60. C. Suresh, H. Nagabhushana, R.B. Basavaraj, G.P. Darshan, D. Kavyashree, B. Daruka Prasad, S.C. Sharma, R. Vanithamani, *$SiO_2@LaOF:Eu^{3+}$ core-shell functional nanomaterials for sensitive visualization of latent fingerprints and WLED applications*, *J. Coll. Inter. Sci.*, 518 (2018) 200-215.
 61. Woo Tae Hong, Jin Young Park, Jae-Yong Je, Hyun Kyoung Yang, *Sintering temperature effect of divalent europium ion doped tetra-calcium phosphate phosphors for latent fingerprint detection*, *Opt. Mat.*, 81 (2018) 37-44.

62. H.S. Yogananda, R.B. Basavaraj, G.P. Darshan, B. Daruka Prasad, Ramachandra Naik, S.C. Sharma, H. Nagabhushana, New design of highly sensitive and selective $\text{MoO}_3:\text{Eu}^{3+}$ micro-rods: Probing of latent fingerprints visualization and anti-counterfeiting applications, *J. Coll. Inter. Sci.*, 528 (2018) 443-456.
63. R.B. Basavaraj, G.P. Darshan, B. Daruka Prasad, S.C. Sharma, H. Nagabhushana, Rapid visualization of latent fingerprints using novel $\text{CaSiO}_3:\text{Sm}^{3+}$ nanophosphors fabricated via ultrasound route, *J. Rare Earths*, <https://doi.org/10.1016/j.jre.2018.04.019>.
64. M. Wang, Y. Zhu, C. Mao, Synthesis of NIR-Responsive $\text{NaYF}_4:\text{Yb}$, Er Upconversion fluorescent nanoparticles using an optimized solvothermal method and their applications in enhanced development of latent fingerprints on various smooth substrates, *Lang.*, 31 (2015) 7084-7090.
65. J.Y. Park, H.K. Yang, Novel red-emitting $\text{Y}_4\text{Zr}_3\text{O}_{12}:\text{Eu}^{3+}$ nanophosphor for latent fingerprint technology, *Dyes Pigm.*, 141 (2017) 348-355.
66. M. Wang, M. Li, A. Yu, J. Wu, C. Mao, Rare Earth fluorescent nanomaterials for enhanced development of latent fingerprints, *ACS Appl. Mater. Interfaces*, 7 (2015) 28110-28115.
67. Y. Kim, H. Jung, J. Lim, S. Ryu, J. Lee, Rapid imaging of latent fingerprints using biocompatible fluorescent silica nanoparticles, *Lang.*, 32 (2016) 8077-8083.
68. H. Chen, R. Ma, Y. Chen, L. Fan, Fluorescence development of latent fingerprint with conjugated polymer nanoparticles in aqueous colloidal solution, *ACS Appl. Mater. Interfaces*, 9 (2017) 4908-4915.
69. Y. Chen, S. Kuo, W. Tsai, C. Ke, C. Liao, C. Chen, Y. Wang, H. Chen, Y. Chan, Dual colorimetric and fluorescent imaging of latent fingerprints on both porous and nonporous surfaces with near-infrared fluorescent semiconducting polymer dots, *Anal. Chem.*, 88 (2016) 11616-11623.
70. Y. Yu, L. Yan, Z. Xia, Non-toxic luminescent Au Nanoclusters@Montmorillonite nanocomposites powders for latent fingerprint development, *RSC Adv.*, 7 (2017) 50106-50112.
71. J. Wang, N. He, Y. Zhu, Z. An, P. Chen, C.A. Grimes, Z. Nie, Q. Cai, Highly-luminescent Eu, Sm, Mn-doped CaS up/down conversion nano-particles: application to ultra-sensitive latent fingerprint detection and in vivo bioimaging, *Chem. Commun.*, 54 (2018) 591-594.
72. Kapil Kumar, Harminder Singh, Vanita Vanita, Ramesh Singh, Khashti Ballabh Joshi, Gaurav Bhargava, Subodh Kumar, Prabhpreet Singh, *Sens. Actuators, B*, 283 (2019) 651-658.

- Fig.1 (a) Schematic representation of probable crystallization mechanism in ultrasonication method and (b) LFPs visualization technique using optimized $\text{YAlO}_3:\text{Ce}^{3+}$ (5 mol %) NPs followed by powder dusting method under UV 254 nm light.
- Fig.2 (a & b) PXRD profiles and W-H plots of $\text{YAlO}_3:\text{Ce}^{3+}$ (1-11 mol %) NPs, (c) variation of crystallite size for different Ce^{3+} ions concentration, and (d) FTIR spectra of the prepared samples.
- Fig.3. Proposed three-step pathway for $\text{YAlO}_3:\text{Ce}^{3+}$ (5 mol %) NPs nucleation in solution.
- Fig.4. Plausible mechanism for the formation of hierarchical nanostructures.
- Fig.5. Probable growth mechanism of hierarchical $\text{YAlO}_3:\text{Ce}^{3+}$ (5 mol %) architectures in the presence of EGCG.
- Fig.6. SEM images of $\text{YAlO}_3:\text{Ce}^{3+}$ (5 mol %) NPs prepared by varying ultrasound irradiation time (1-6 h).
- Fig.7. SEM images of $\text{YAlO}_3:\text{Ce}^{3+}$ (5 mol %) NPs prepared by varying concentration of EGCG (5-30 % W/V) while ultrasound irradiation time fixed at ~ 6 h.
- Fig.8 (a) TEM, (b) HRTEM image, (c) SAED pattern and (d) Enlarged view of HRTEM of $\text{YAlO}_3:\text{Ce}^{3+}$ (5 mol %) NPs.
- Fig.9 (a) PL excitation, (b) PL emission spectra, (c) graph of concentration versus PL intensity to showing concentration phenomena, (d) logarithmic plot of concentration (x) and (I/x), (e) CIE and (f) CCT diagram of $\text{YAlO}_3:\text{Ce}^{3+}$ (1-11 mol %) NPs.
- Fig.10. FPs visualized by staining $\text{YAlO}_3:\text{Ce}^{3+}$ (5 mol %) NPs on various coloured background porous surfaces after illumination of UV 254 nm light.
- Fig.11 (a-c) Visualized FPs by staining TiO_2 , Fe_2O_3 , $\text{YAlO}_3:\text{Ce}^{3+}$ (5 mol %) NPs on glass surfaces and (d-f) FPs aged on glass surface for various periods of time (1, 7, 20 and 30 days), stained by $\text{YAlO}_3:\text{Ce}^{3+}$ (5 mol %) NPs.
- Fig.12. FPs visualized by using optimized $\text{YAlO}_3:\text{Ce}^{3+}$ (5 mol %) NPs on various non-porous surfaces excited by UV 254 nm light.
- Fig.13. FPs visualized by using optimized $\text{YAlO}_3:\text{Ce}^{3+}$ (5 mol %) NPs on glass surfaces and its defined ridge characteristics excited by UV 254 nm light. The scale bar corresponds to 2.5 mm.
- Fig.14. Anti-mimetic patterns drawn by simple dip pen mode using optimized $\text{YAlO}_3:\text{Ce}^{3+}$ (5 mol %) NPs excited by normal and UV 254 nm light. The scale bar corresponds to 5 mm.

Table.1. Estimated crystallite size and lattice strain of $\text{YAlO}_3:\text{Ce}^{3+}$ (1-11 mol %) NPs.

Ce^{3+} (mol %)	Average crystallite size (nm)		Strain ϵ ($\times 10^{-3}$)
	Scherrer's method	W-H Plots	
1	34	32	1.7
3	37	35	1.8
5	40	39	1.5
7	43	42	1.4
9	45	44	1.3
11	48	47	1.6

Table.2. Various nanomaterials utilized for visualization of LFPs by many authors.

SL. No.	Sample	Synthesis technique	Emission color	References
1	$\text{La}_2\text{Ti}_2\text{O}_7:\text{Eu}^{3+}$	Solvothermal	Red	Jin Young Park et al. [55]
2	$\text{Ba}_3\text{V}_2\text{O}_8$	Wet-chemical	Green	Krishna Bharat et al.[56]
3	$\text{TiO}_2:\text{Eu}^{3+}$	Hydrothermal	Red	Venkatesha Babu et al.[57]
4	$\text{BaTiO}_3:\text{Eu}^{3+}$	Combustion	Red	Dhanalakshmi et al.[58]
5	$\text{Sr}_{10}(\text{PO}_4)_6\text{O}:\text{Ce}^{3+}$	Solid state	Cyan blue	Park et al.[59]
6	$\text{SiO}_2@\text{LaOF}:\text{Eu}^{3+}$	Solvothermal	Red	Suresh et al. [60]
7	$\text{Ca}_4(\text{PO}_4)_2\text{O}:\text{Eu}^{2+}$	Ball milling	Blue	Hong et al.[61]
8	$\text{MoO}_3:\text{Eu}^{3+}$	Sonochemical	Red	Yogananda et al.[62]
9	$\text{CaSiO}_3:\text{Sm}^{3+}$	Sonochemical	White	Basavaraj et al.[63]
10	$\text{YAlO}_3:\text{Ce}^{3+}$	Sonochemical	Cyan blue	Present work

Table.3. Comparison of FP results reported in the previous works with present study.

Hosts	Method of Synthesis	Method of FP detection	Types of surfaces used for detection	FP detection	References
NaYF ₄ :Yb, Er	Solvothermal (180 °C/24 h)	Powder dusting	Ceramic tile, marble, glass (Non-porous) Note papers, Chinese paper money, and plastic plates (Porous)	Type I and II	Wang et al. [64]
Y ₄ Zr ₃ O ₁₂ :Eu ³⁺	Solvothermal (1000 °C/5 h)	Powder dusting	Aluminum foil, plastic tube (Porous) glass, compact disk, stainless steel (Non-porous)	Type I and II	Park et al. [65]
YVO ₄ :Eu, LaPO ₄ :Ce,Tb	Hydrothermal (180 °C/24 h)	Powder dusting	Plastic cards, aluminum alloys sheets, printing papers (Porous) Ceramic tiles, marbles, painted wood, and floor (Non-porous)	Type I and II	Wang et al. [66]
Fluorescent SiO ₂	Stöber method	Mild air flow	Glass (Non-porous)	Type I and II	Kim et al. [67]
Poly(p-phenylene vinylene) (PPV) NPs	Modified Wessling (80 °C / 3h)	Immersing	Adhesive tape (Porous)	Type I and II	H. Chen et al. [68]
Fluorescent Semiconducting Polymer Dots	Suzuki coupling reaction (100 °C /48 h)	Spraying	Printing paper and colored paper (Porous) Glass, aluminum foil, plastic bag, and acrylic sheet (Non-porous)	Type I, II and III	Y. Chen et al. [69]
AuNCs@MMT	One-pot microwave 35 °C under vacuum condition	Powder dusting	Weighing paper, adhesive tape (Porous) Binder clips, slide glass, transparent tweezers and porcelain enamel (Non-porous)	Type I, II and III	Y. Yu et al. [70]
CaS:Eu,Sm,Mn	Reverse microemulsion	Powder dusting	Foil and plastic substrates (Porous) Tile and glass (Non-porous)	Type I and II	J. Wang et al. [71]

Coronenediimide	Dissymmetric bay	Solution spray and powder dusting	Paper sheets (Porous) Aluminium, stainless steel, glass, metal coins, compact discs (CDs), OHP films, ceramic tiles (Non-porous).	Type I and II	Kapil Kumar et al [72]
YAlO ₃ :Ce ³⁺	Sonochemical	Powder dusting	Plastic bottle, plastic sheet, currency, playing cards and crushed aluminum foil (Porous) Glass, marble, metal scale, computer mouse and curved tin bottle surface (Non-porous).	Type I, II and III	Present work

Research highlights

- ❖ Blue emitting $\text{YAlO}_3:\text{Ce}^{3+}$ NPs were prepared via EGCG assisted ultrasonication route.
- ❖ Hierarchical architectures were mainly depending on various reaction parameters.
- ❖ Sweat pores are clearly visualized on various surfaces.
- ❖ The product was highly useful in dermatoglyphics and anti- mimetic applications.

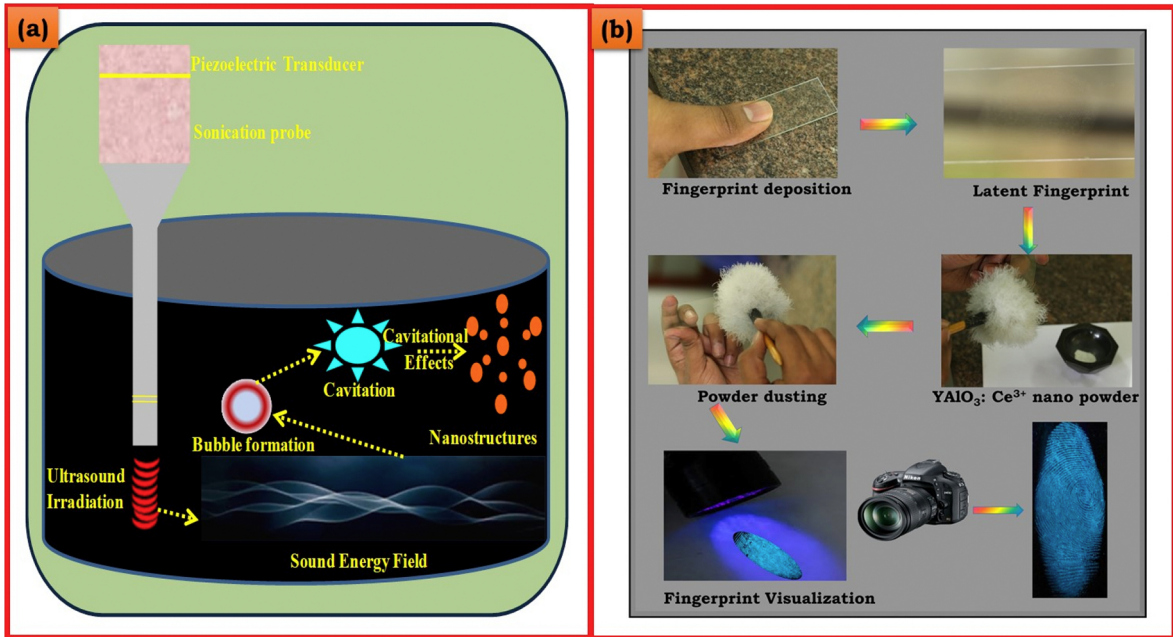


Figure 1

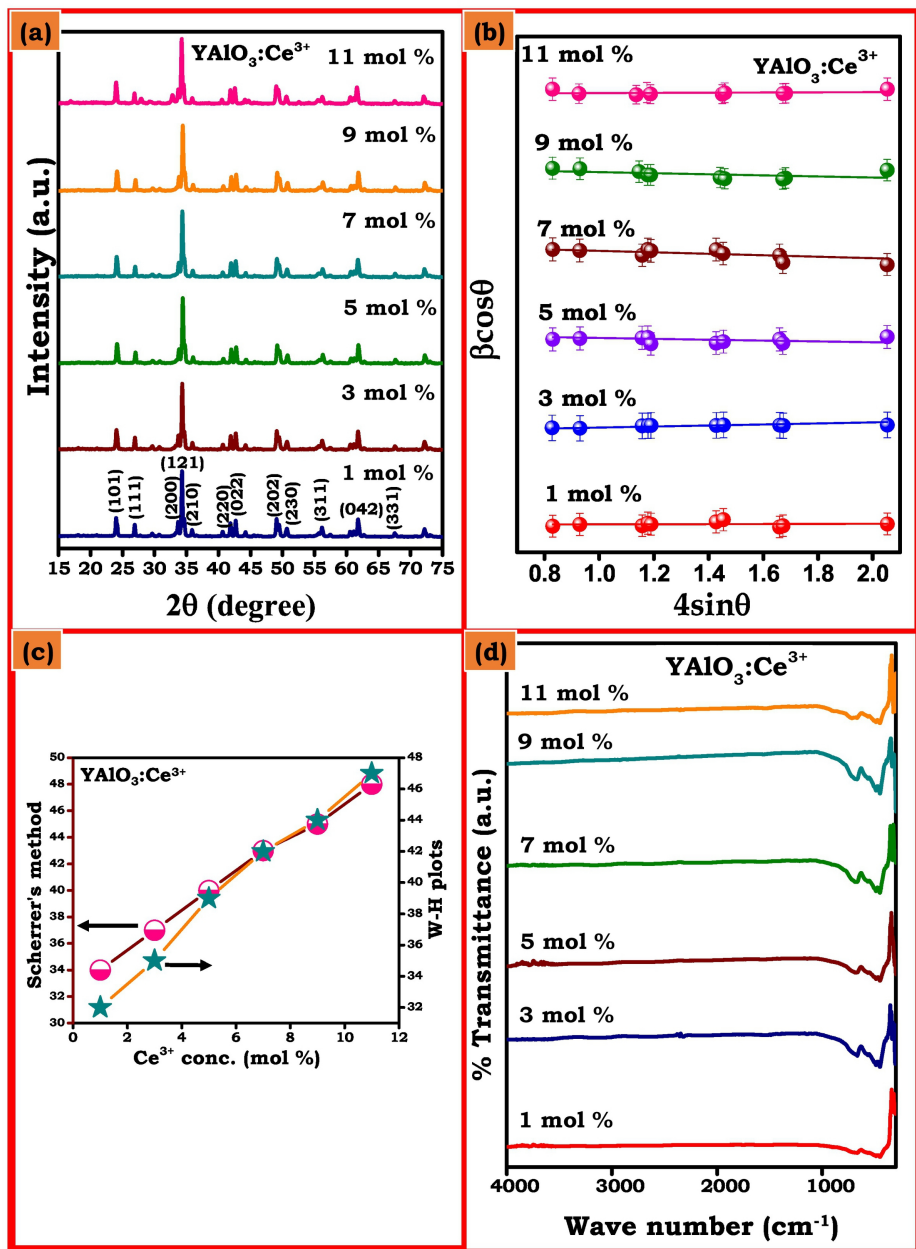


Figure 2

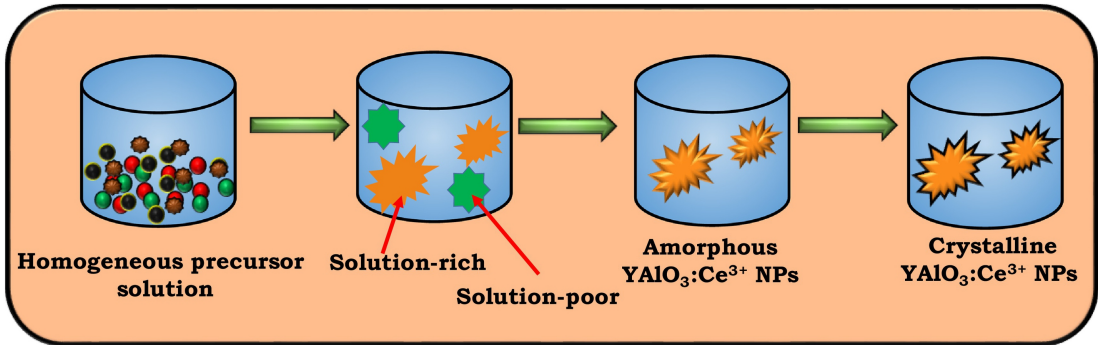


Figure 3

Hierarchical organization

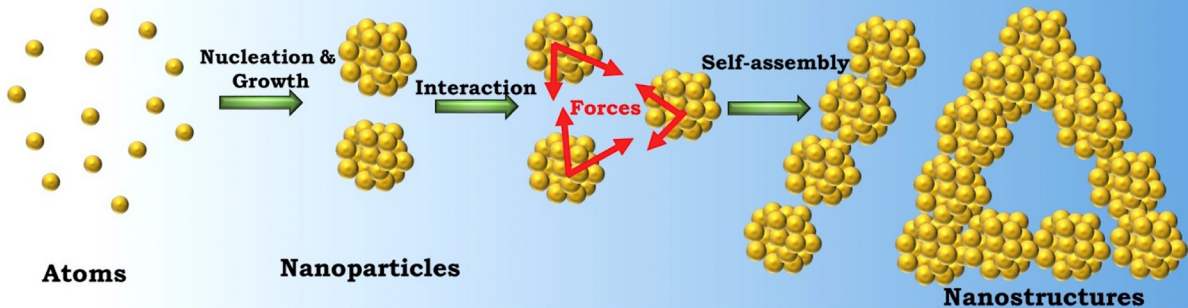


Figure 4

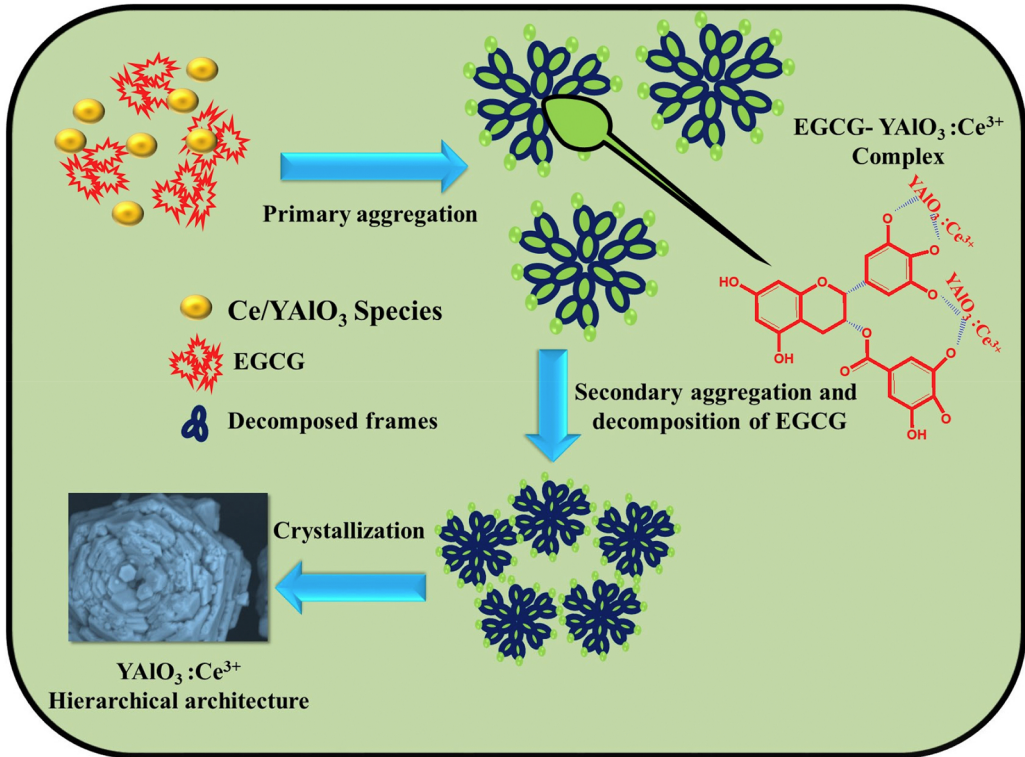


Figure 5

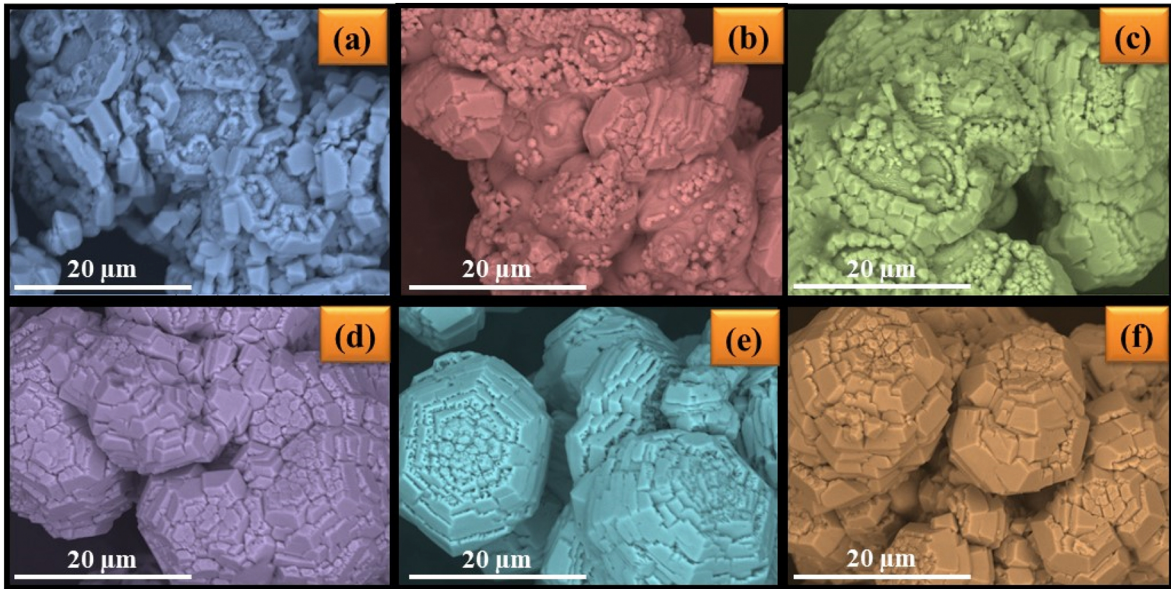


Figure 6

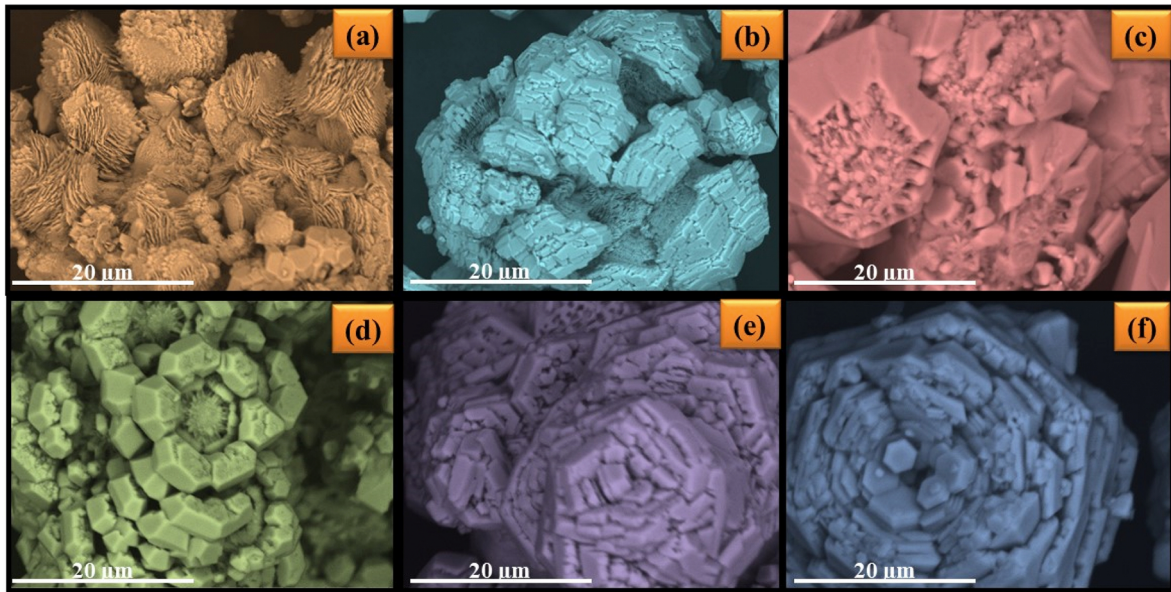


Figure 7

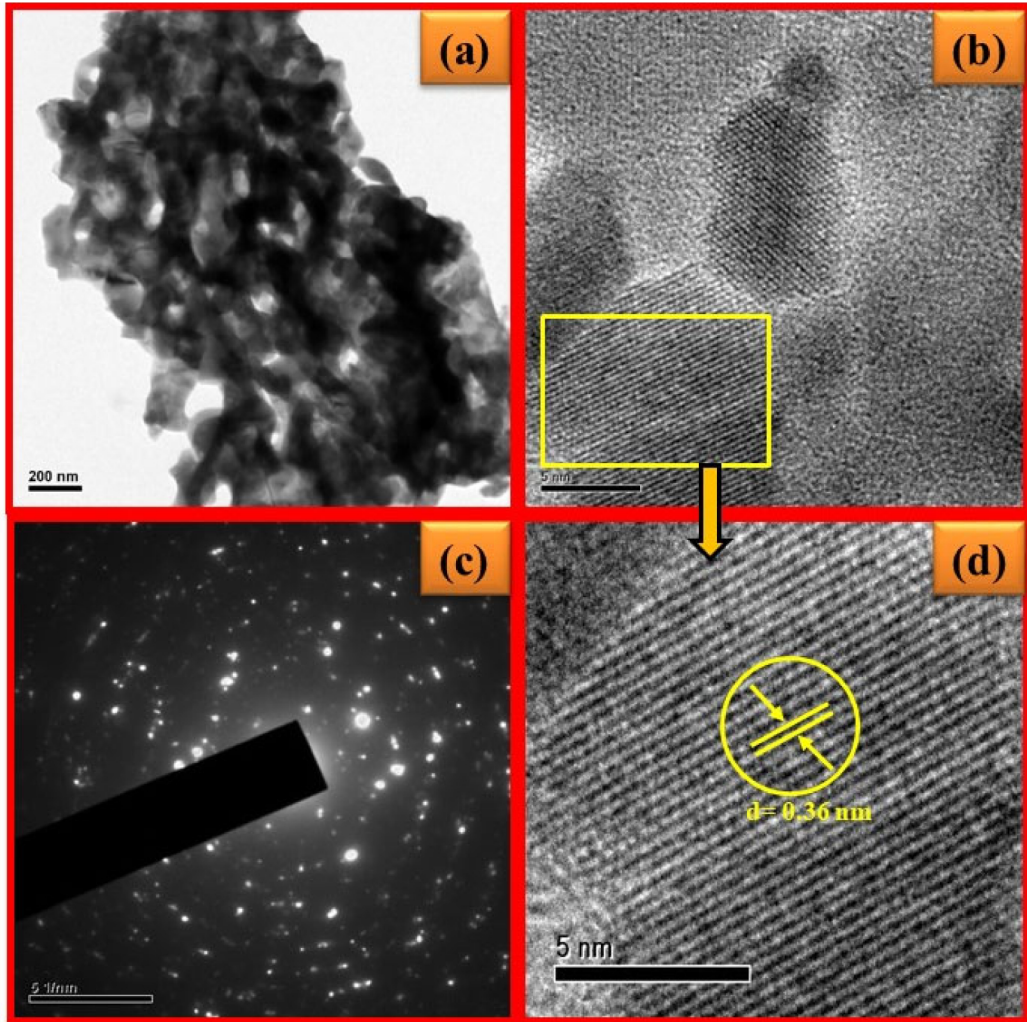


Figure 8

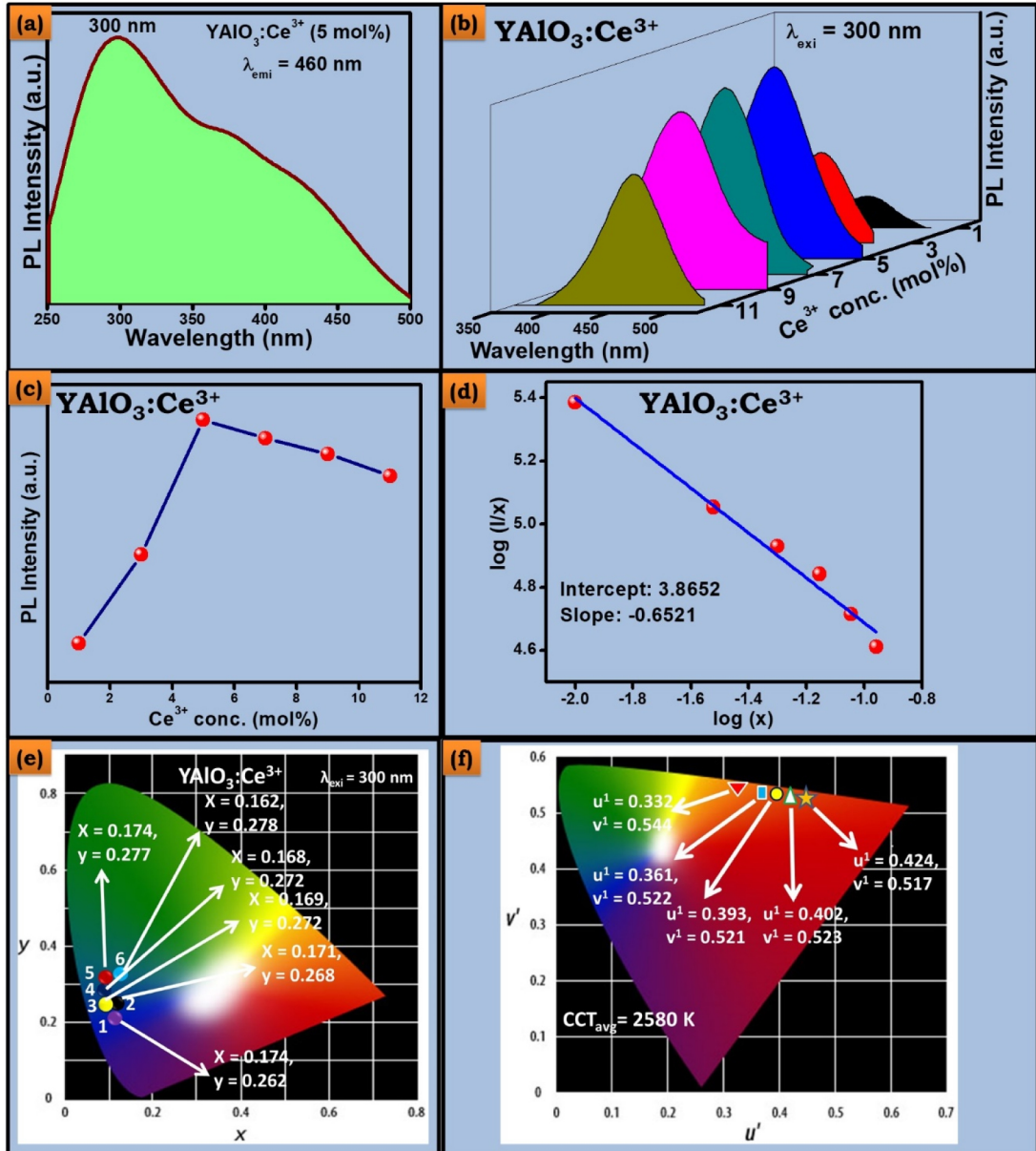


Figure 9

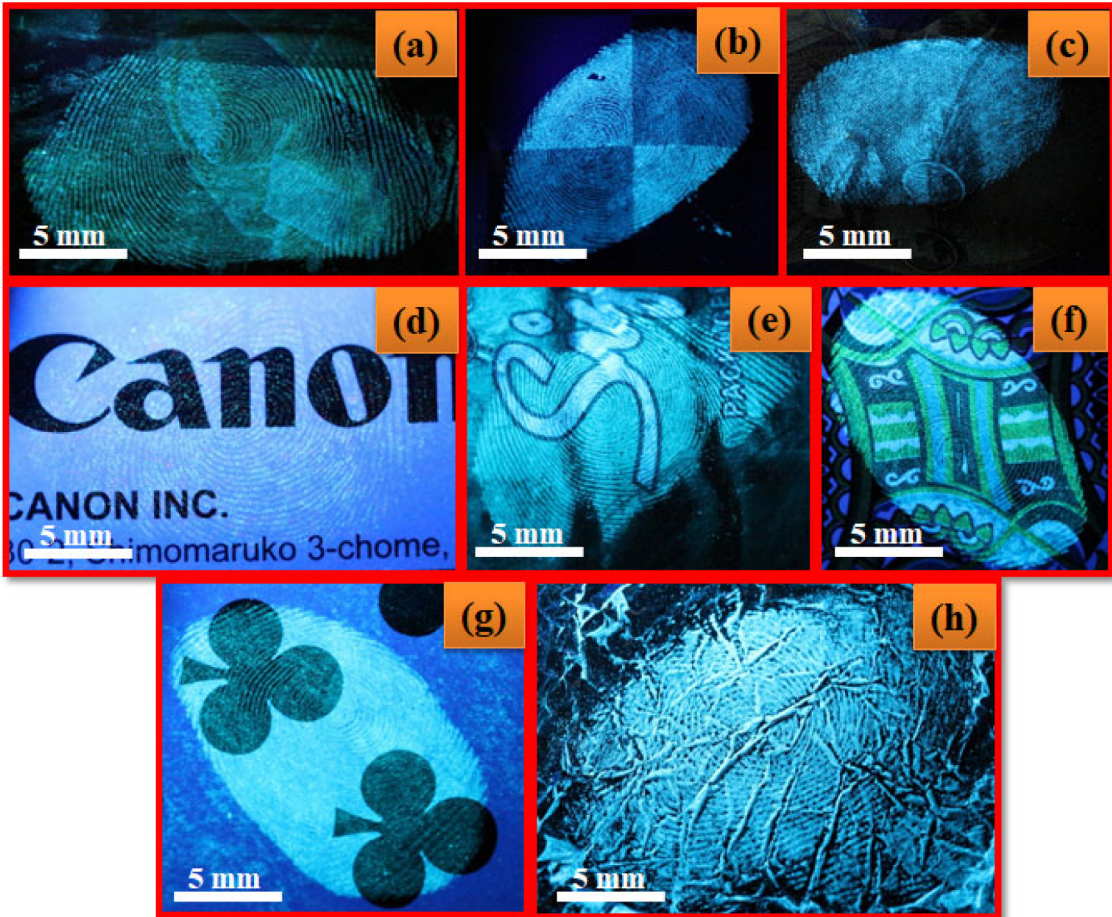


Figure 10

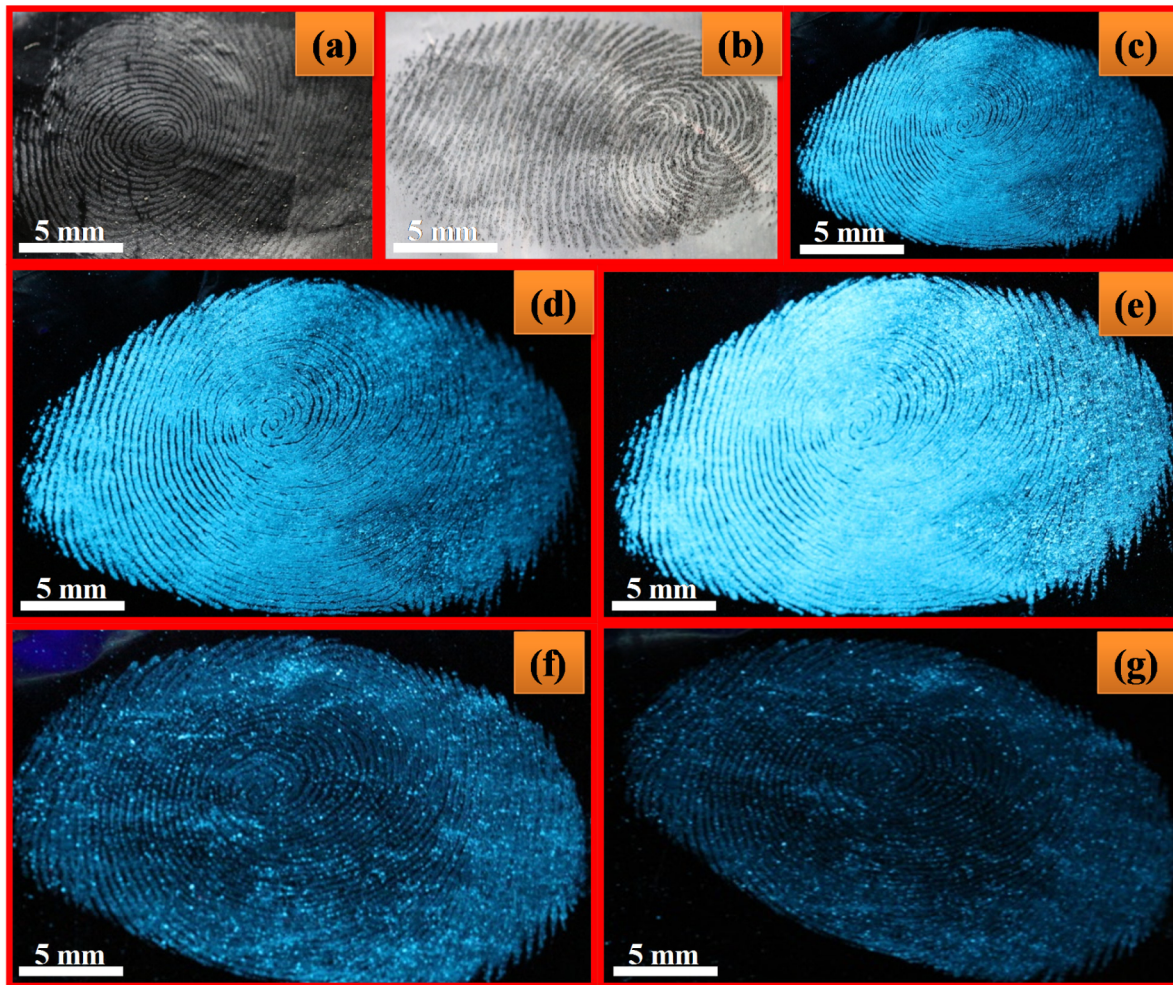


Figure 11

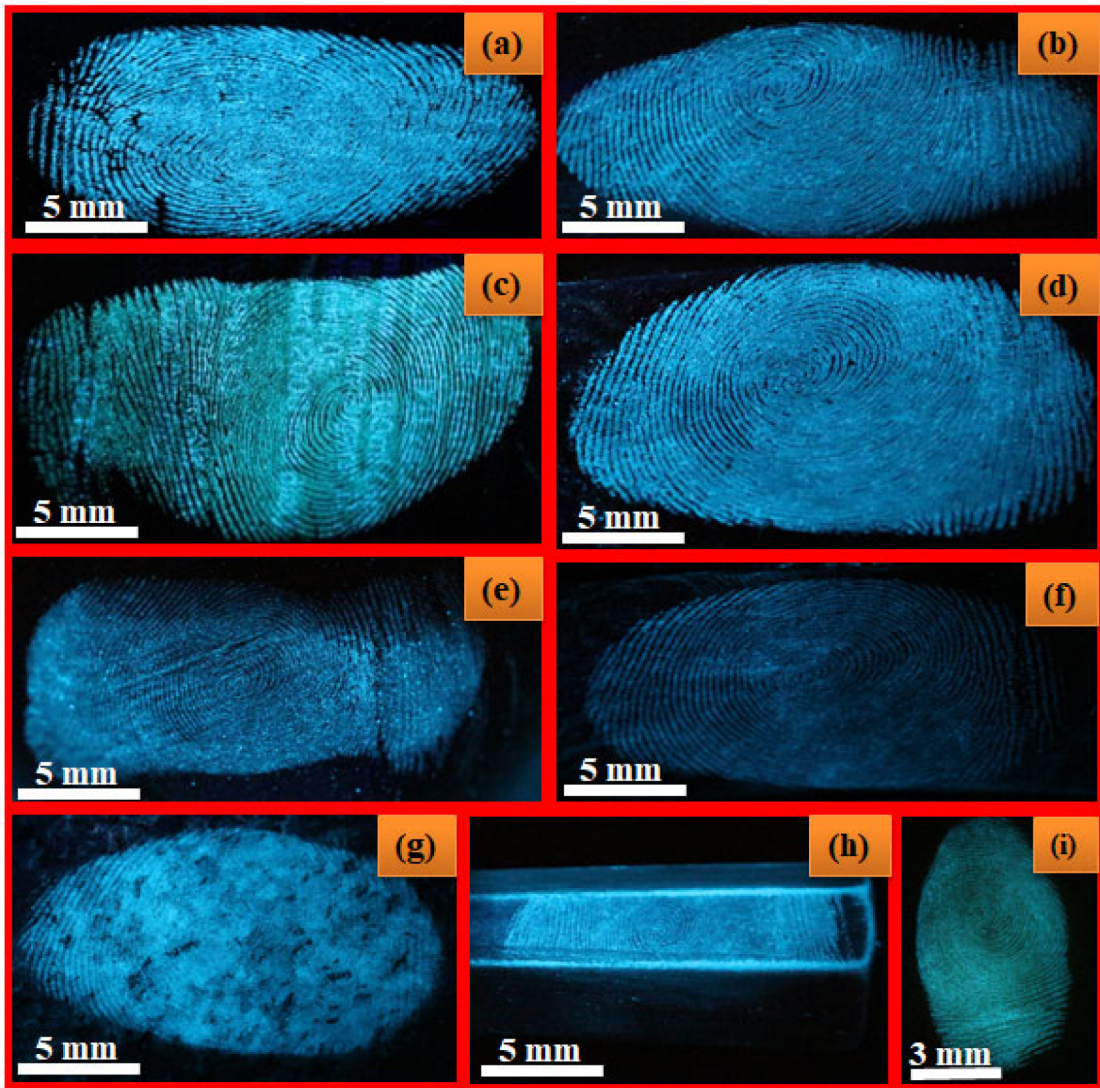


Figure 12

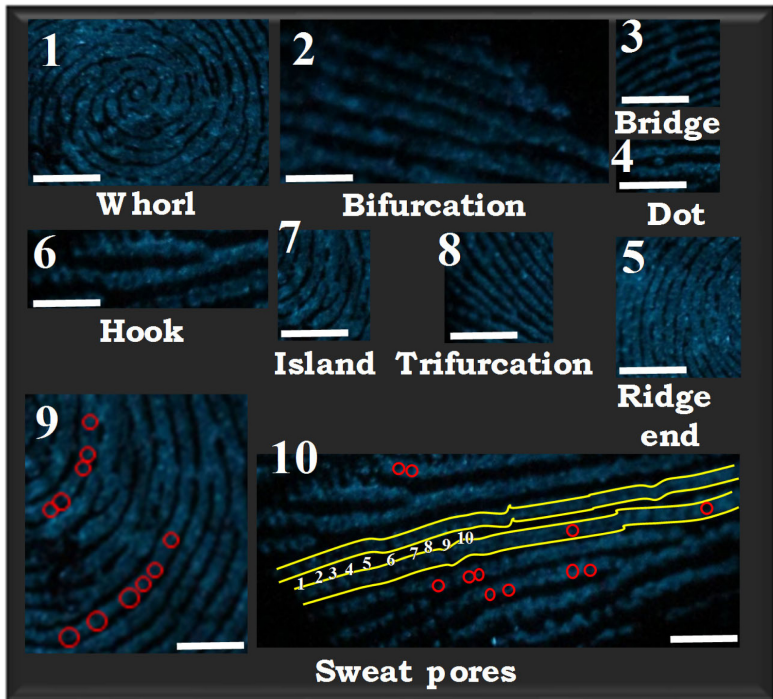
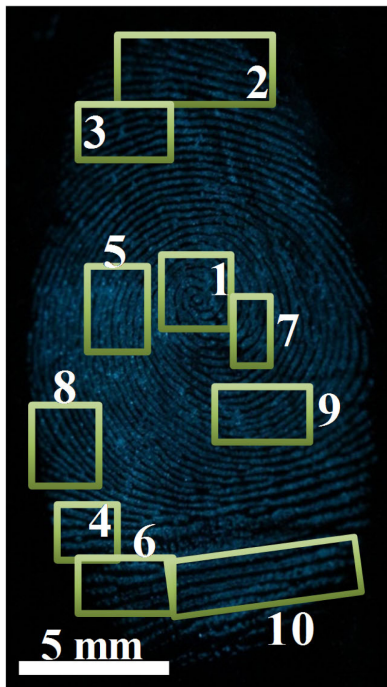


Figure 13

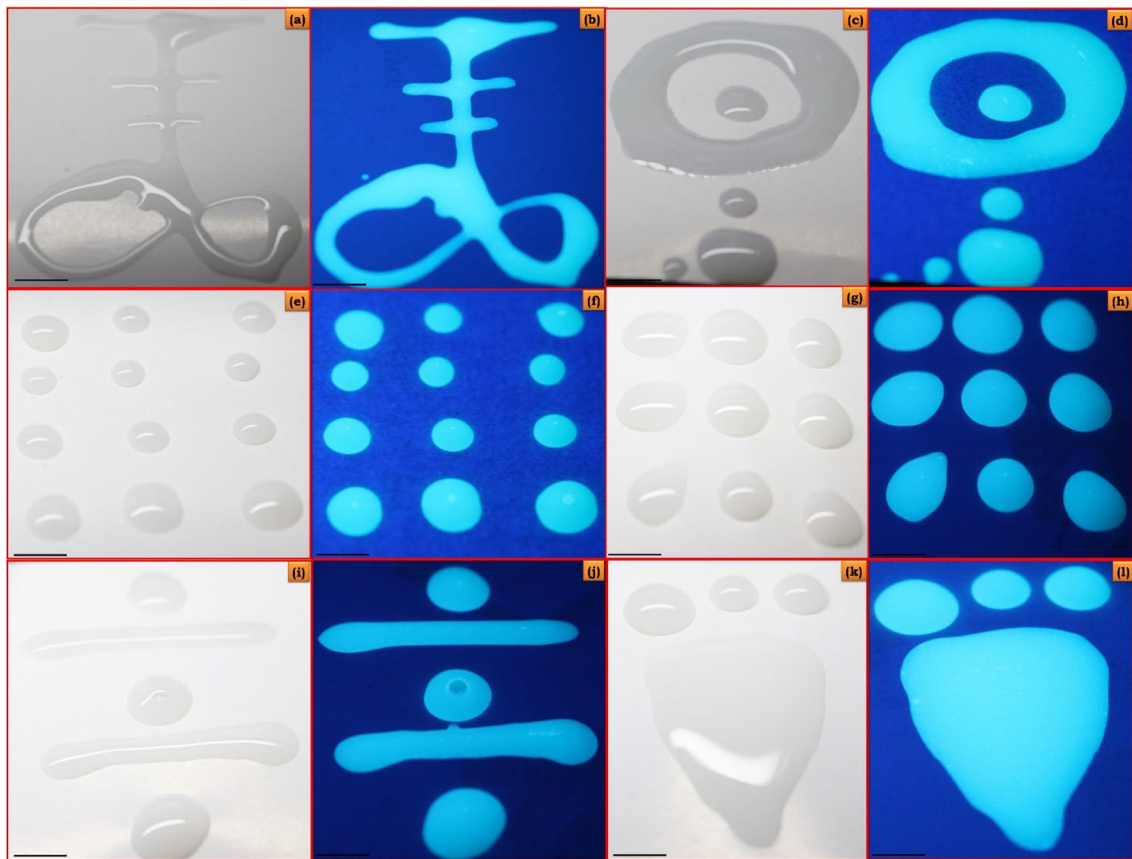


Figure 14